Super-Resolution Axial Localization of Ultrasound Scatter Using Multi-Focal Imaging

Konstantinos Diamantis , Alan H. Greenaway, Tom Anderson , Jørgen Arendt Jensen , *Fellow, IEEE*, Paul A. Dalgarno , and Vassilis Sboros

Abstract—*Objective:* **This paper aims to develop a method for achieving micrometre axial scatterer localization for medical ultrasound, surpassing the inherent, pulse length dependence limiting ultrasound imaging.** *Methods:* **The method, directly translated from cellular microscopy, is based on multi-focal imaging and the simple, aberration-dependent, image sharpness metric of a single point scatterer. The localization of a point scatterer relies on the generation of multiple overlapping sharpness curves, created by deploying three foci during receive processing, and by assessing the sharpness values after each acquisition as a function of depth. Each derived curve peaks around the receive focus and the unique position of the scatterer is identified by combining the data from all curves using a maximum likelihood algorithm with a calibration standard.** *Results:* **Simulated and experimental ultrasound point scatter data show that the sharpness method can provide scatterer axial localization with an average accuracy down to 10.21 μm ($\approx \lambda/21$) and with up to 11.4 times increased precision compared to conventional localization. The improvements depend on the rate of change of sharpness using each focus, and the signal to noise ratio in each image.** *Conclusion:* **Super-resolution axial imaging from optical microscopy has been successfully translated into ultrasound imaging by using raw ultrasound data and standard beamforming.** *Significance:* **The normalized sharpness method has the potential to be used in scatterer localization applications and contribute in current super-resolution ultrasound imaging techniques.**

Index Terms—**Axial localization, beamforming, multiple focusing, normalized sharpness, ultrasound imaging.**

K. Diamantis is with the Institute of Biological Chemistry, Biophysics and Bioengineering, Heriot-Watt University.

A. H. Greenaway, retired, was with the Institute of Biological Chemistry, Biophysics and Bioengineering, Heriot-Watt University.

T. Anderson is with the School of Clinical Sciences, Centre of Cardiovascular Science, University of Edinburgh.

J. A. Jensen is with the Department of Electrical Engineering, Center for Fast Ultrasound Imaging, Technical University of Denmark.

P. A. Dalgarno and V. Sboros are with the Institute of Biological Chemistry, Biophysics and Bioengineering, Heriot-Watt University, Edinburgh EH14 4AS, U.K. (e-mail: P.A.Dalgarno@hw.ac.uk; V.Sboros@hw.ac.uk).

Digital Object Identifier 10.1109/TBME.2017.2769164

I. INTRODUCTION

IN ULTRASOUND imaging, the interference of emitted wavefronts determines the focusing capability of an aperture [1]. The imaging resolution in the lateral direction is limited by diffraction as in all other wavefront based imaging methods, and may vary greatly depending on the beam width and the depth of imaging. On the other hand, the axial resolution is fixed as it only depends on the duration of the transmitted pulses. Therefore, small objects with dimensions in the micrometre range will appear to have a size of the Point Spread Function (PSF), which is comparable to the wavelength (λ) of the applied sound wave [2], [3]. It is feasible to reduce the PSF size by using shorter pulses or transducers with higher central frequency, as well as larger arrays. In practice however, as the frequency is related to attenuation, it is inversely related to penetration depth [1], [4]. As a consequence, there is a trade-off between PSF dimensions and penetration depth. For example, in the axial dimension tissue can be imaged using a transmission of a few MHz, achieving visualization over several centimetres depth, but limiting the axial PSF size to around the millimetre range [4]. Conversely, using several hundreds of MHz can provide PSF sizes in the micrometre range, but with penetration of less than 1 mm [5], [6]. Super-resolution imaging methods are based in the precise localization of single scatterers. Not only do these methods offer improved image quality for greater penetration depths but also, by providing access to exact scatterer positioning and thus velocities, they enable scatter density and dynamics measurements that directly relate to blood volume and blood flow quantification respectively. This leads directly to additional benefits across ultrasound imaging in diagnostic applications [7].

Super-resolution imaging is well-established in other fields of sensing [8] such as radar [9]–[11], astronomy [12], and optical microscopy [13]–[15], however in ultrasound imaging it remains in its infancy. In general super-resolution ultrasound is connected to contrast enhanced ultrasound (CEUS), which is based on the use of contrast microbubbles (MBs). It has been established that despite the small size of the MBs (1–10 μm diameter), it is possible to distinguish single scattering events due to their high scattering cross-section [16]. CEUS methods therefore have a direct analogy with single molecule microscopy modalities, where single scattering events are replaced with single point emission events. Modern imaging and signal processing enables the visualization of MB signals as they flow through the vascular bed [17]. However, the requirement

to use high concentrations of MBs produces images that, for clinical applications, allow only the varying brightness to provide a qualitative assessment of vascular kinetics. CEUS is therefore, not only diffraction limited, but generally qualitative with limited potential to advance into robust quantitative measurements of the blood flow dynamics. Positron Emission Tomography (PET), Magnetic Resonance Imaging (MRI) and contrast Computed Tomography (CT), all provide an improved quantitative assessment of perfusion and thus are often the technologies of choice in the clinic when deemed cost effective. However, ultrasound is fast, safe, easy to use and generally, highly cost effective. CEUS provides the foundation for super-resolution ultrasound imaging which, to a large extent, is based on the utilization of contrast MBs. Techniques have focused on the resolution improvement achievable by imaging single MBs relying on *a priori* knowledge of the MB as a point scatter. Such methods provided localization based super-resolution, comparable to Photoactivated Localization Microscopy (PALM) and Stochastic Optical Reconstruction Microscopy (STORM) techniques, and showed that more detailed and robust measurements of blood flow dynamics may be obtained.

By using this knowledge, *O'Reilly and Hynynen* have been able to obtain high resolution transcranial images of vascular structure [18], [19] that were of similar quality to those acquired by micro-CT. Further, *in-vivo* imaging of the mouse ear microvasculature with 5-fold resolution gains have been demonstrated by *Christensen-Jeffries et al.* with the additional feature of a super-resolution velocity map [20]. *Couture et al.* demonstrated the ultrasound equivalent of optical localization microscopy, Microbubble Ultrasound Super-Localization Imaging (MUSLI), which can achieve individual MB lateral localization with up to $\lambda/38$ accuracy [21], [22]. Similarly, *Desailly et al.* presented the analog of fluorescence PALM (f-PALM) in ultrasound imaging, ultrafast Ultrasound Localization Microscopy (uULM) [23], [24]. By using uULM, *Errico et al.* were able to achieve *in-vivo* imaging and haemodynamic quantification of $\leq 10\,\mu$m-diameter rodent cerebral microvessels [7]. Finally, *Ackermann and Schmitz* estimated single microbubble positions by applying foreground detection and a modified Markov Chain Monte Carlo data association (MCMCDA) algorithm [25]. This allowed the reconstruction of vessels beyond the conventional resolution limits.

These attempts demonstrate the potential for super-resolution ultrasound imaging. However, the image formation used in ultrasound equipment is designed for structural/anatomical imaging. The ultrasound super-resolution techniques above, with the exception of uULM [7], [23], [24], are applied to already beam-formed images, which is vulnerable to image quality variations, including the highly variable PSF, the noise, and a number of artefacts encountered in the ultrasound image. A more robust approach to improve quality and spatial resolution involves wavefront modification and adaptive array beamforming. For example, the re-emission of the received transducer element responses can compensate for the wavefront distortion, caused by the changing impedance mismatch between the transducer face and the target material [26]–[28]. Alternatively, various adaptive beamforming approaches have shown that up to $\lambda/12$ lateral resolution in the localization of isolated point scatterers can be

achieved [29], [30], and there is an early demonstration using raw ultrasound data from *in-vivo* measurements [31]. The results show that particularly Minimum Variance (MV) beamforming could be suited to the detection of vessel stenosis [32], and to real-time cardiac ultrasound imaging [33], providing improved lateral resolution.

The above approaches demonstrate significant research effort to generate ultrasound imaging methods for improving the lateral resolution, which due to its dependence to focusing is subject to improvement beyond the conventional limits. However, there is very little work on improvements in the axial dimension in the localization of a single point reflector. Inherently this is more challenging due to the strict dependence of the axial PSF size on the Spatial Pulse Length (SPL) which is constant. The SPL is given by $n_{cy} \times \lambda$, where n_{cy} is the number of cycles in the ultrasound pulse. Thus, axial super-resolution is currently only dealt by the few image analysis approaches described above [7], [18]–[25]. In this work, a new signal-based method for precise axial ultrasound point scatter localization is introduced. The method, based on simultaneous imaging using multiple foci, originates from optical microscopy, which also suffers from the complex nature of the PSF. Beamforming is used to acquire multiple axially displaced images of single point source emitters, and image sharpness is used to convert these images into a high precision axial localization co-ordinate. Image sharpness, the integrated square intensity over the emitter, has been shown to be a viable method to expand the lateral super-resolution [34]–[36] to the axial dimension [37], [38], in the optical analogy. It is a simple metric that represents any deviation from an in-focus image [39]–[41], and when combined with a multi-focal imaging system [42] and a maximum likelihood estimation (MLE), has been used in optical systems to extract axial localization precision below 10 nm, or $\lambda/50$ [43], [44]. In this paper, these techniques are translated into ultrasound imaging. The feasibility of the method is investigated using a simple point reflector experimental setup.

II. METHODS

A general overview of the proposed method which was used for axial localization of isolated ultrasound point scatterers is depicted in Fig. 1. The ultrasound transmissions [see Fig. 1(a)] provide the point scatter data at different depths. These data are processed in multiple ways in receive as shown in Fig. 1(b). The normalized sharpness is calculated for all scatterer positions and receive foci, creating multiple (equal to the number of receive foci) sharpness references for each axial position. These sharpness values are then translated into axial position estimates, with micrometre deviations from the true scatterer positions as shown in in Fig. 1(c).

A. Image Sharpness

The metric of image sharpness can be seen as a single descriptor of total PSF aberration. As it is the highest order aberration, sharpness is dominated by defocus, with out of focus images presenting lower sharpness values. Lower order aberrations present a small perturbation to the defocus change, and can thus be ignored. Sharpness thus provides a single
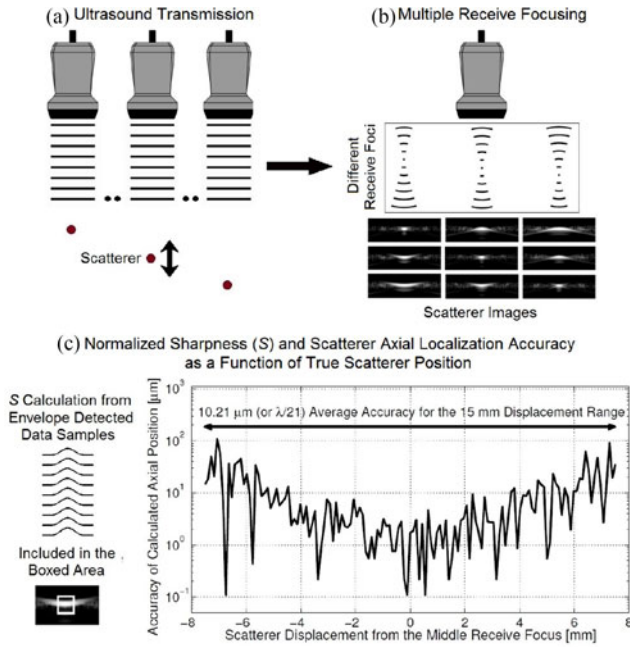
Fig. 1. Description of the proposed sharpness-based axial localization method. (a) The ultrasound reflection of a scatterer at a specific depth in the field is acquired. This is repeated at several depths. (b) The data are then beamformed offline with three receive foci. (c) The calculation of sharpness uses data from a small Region of Interest (ROI). The calculation is repeated for all scatterer images, leading to high precision axial localization.

quantifiable metric linked to particle defocus position. There is no unique mathematical definition of image sharpness, but generally it involves the integration under the square of the modulation transfer function. In practice this simplifies to the sum of the square of the pixel intensities, with the exact formulation tailored or optimized to the application [39]–[41]. A similar to image sharpness concept was earlier employed in ultrasound imaging relating speckle brightness to optimum focusing [45]. In the previous optical work [44] a normalized version of image sharpness, S_{opt}, was used and defined as:

$$S_{opt} = \sum_{k=1}^{K}(n_k^2 - n_k)/\left(\sum_{k=1}^{K} n_k\right)^2, \qquad (1)$$

for an image within a window consisting of K pixels where n_k is the recorded intensity of the k-th pixel of the window. The subtraction in the numerator is to eliminate photon bias in the low-flux regime, where intensities are expressed in photon counts, and has negligible effect at modest to high-flux. The calculation of sharpness is similar for an ultrasound image containing a single point target, but the subtraction is neglected, since data are not flux-dependent. In ultrasound imaging it is possible to access the raw Radio Frequency (RF) data from which the final image is created and avoid distortions associated to the image formation stage (i.e. interpolation, logarithmic compression). Upon signal acquisition the Hilbert Transform provides the signal envelope and the subsequent rectification generates a pre-image signal, free from image processing bias. As a result

the pixel intensity, which is proportional to the square of the signal amplitude, may also be substituted with the latter quantity, for an alternative ultrasound sharpness derivation, given by:

$$S = \sum_{q=1}^{Q} |E_q|^4 / \left(\sum_{q=1}^{Q} |E_q|^2\right)^2, \qquad (2)$$

where S is the normalized ultrasound sharpness and $|E_q|^2$ is the squared amplitude value of the q-th sample. The amplitude was derived using envelope detected data. However, there is no practical difference between the raw and envelope detected data due to the use of only even powers of $|E_q|$ in (2). The metric is calculated over Q samples in total, including a single point scatterer. The region of interest (ROI) is defined as a square box around the PSF centre and of a size adequate to encompass the PSF main lobe at all defocus conditions. Larger ROIs enclosing the whole PSF are not necessary for the sharpness calculation, while they are also likely to include undesired overlapping information in the presence of multiple scatterers.

B. Beamforming

In *Dalgarno et al.* [43] and *Dalgarno et al.* [44] image sharpness was used as an adjunct to multi-plane (multi-focal) microscopy, to demonstrate axial super-resolution potential for live cell axial imaging. As sharpness peaks at focus and falls, approximately symmetrically either side of focus, a single plane gives an ambiguous dissemination of position with one sharpness value corresponding to two axial positions [44]. Furthermore, there is zero dependence around focus, where the sharpness peak has poor correlation with position. Multi-plane microscopy, where distinct focal planes are imaged simultaneously, removes the ambiguity by providing multiple references to translate sharpness to an absolute axial position. To achieve this optically, a distorted diffraction grating [42] was paired with a relay lens and used as an attachment to a standard optical microscope. The same principle can be directly applied to ultrasound imaging, however multiple focusing can be achieved by conventional beamforming without requiring additional hardware, and is therefore considerably simpler to implement than the optical equivalent. In the ultrasonic case the receive focus provides higher flexibility compared to transmit focusing, as the element signals can be stored after the transmission and beamformed offline, or even in real time, in multiple ways. The conventional method to process the received transducer element signals is the Delay-And-Sum (DAS) beamformer [46]. The signals are time-delayed, weighted, and subsequently summed to form the maximized beamformer output, $B(t)$. For a transducer array with M active elements in receive $B(t)$ can be extracted by:

$$B(t) = \sum_{m=0}^{M-1} w_m(t)x_m(t - \tau_m) = \mathbf{w}(t)^H X(t), \qquad (3)$$

where t is the time index, $\mathbf{w}(t) = [w_0(t), w_1(t), \ldots, w_{M-1}(t)]^H$ is the vector of the apodization weights, $X(t) = [x_0(t - \tau_0), x_1(t - \tau_1), \ldots, x_{M-1}(t - \tau_{M-1})]^H$ is the array of the transducer element signals, and τ_m is the time delay applied to the

m-th receive element, depending on its distance from the selected focus point. Therefore, $B(t)$ can be calculated for different focus points simply by changing the time delays, and in this way the requirement for simultaneous axially displaced images in [43], [44] can be easily met. In this work, three different receive foci will be selected, with each of the three beamformer outputs producing a different, but axially displaced, image of the same object.

C. Maximum Likelihood Estimation

The MLE is an established statistical method to estimate the parameters of a dataset to a known model. It was employed in the optics approach [44] to extract the axial location of a single point scatterer using known calibration data. Applied to the multi-focal imaging method, the estimate is unique, since each position is characterized by three, or more, distinct sharpness values dependent on the number of imaging planes employed. The calibration data can be obtained from repetitive measurements of point scatterers moving in depth under equivalent experimental conditions. This enables the calculation of the standard deviation of the measured mean sharpness at each position. The mean sharpness plotted over the point scatterer axial distance typically forms a Lorentzian-like sharpness curve (*S*-curve) that peaks around the best focus position. Although the standard deviation does not follow any specific trend, higher values are present around the peak of an *S*-curve and lower at the edges. Both statistical measures are interpolated by a factor I, to provide sub-resolution sampling and reduce inaccuracies due to quantization.

The interpolated data are then used for the estimation of the probability density function (PDF), $P(S_j|z)$. This is the probability that a specific normalized sharpness value, S_j, will be measured from the raw scatter data of a point scatterer located at depth z, where j denotes the focus in receive. Since the sharpness calculations for each receive focus do not depend on each other and with the calibration z known, the probability for the set of N sharpness measurements for all receive foci, when a point scatterer is located at z, can be expressed as:

$$L(S_1, S_2, \ldots, S_N|z) = \prod_{j=1}^{N} P(S_j|z), \qquad (4)$$

where L is the likelihood for the set of sharpness measurements $S_1, S_2, \ldots, S_N$ and N is the number of the receive foci. The maximum likelihood estimator of the point depth, z, is the value of z for which L is maximized given an actual dataset $S_1, S_2, \ldots, S_N$ and the calibration PDFs, $P(S_j|z)$. For the PDF a Gamma distribution is selected as it fits best with the Lorentzian shaped *S*-curves and their variance, and is given by:

$$P(S_j|z) = \frac{e^{\bar{S}_j^2} \bar{S}_j^{\alpha-1}(z)\beta^{-\alpha}}{\Gamma(\alpha)}, \qquad (5)$$

where $\alpha = \bar{S}_j^2(z)/\bar{\sigma}_j^2$, $\beta = \bar{\sigma}_j^2/\bar{S}_j^2(z)$, $\bar{S}_j(z)$ represents the interpolated *S*-curve, $\bar{\sigma}_j^2$ the interpolated variance, and Γ is the Gamma function. The MLE solution, by substituting (5) into (4), is the point scatterer z depth for which the product of the N Gamma distributions is maximized.

D. Data Analysis

A set of three sharpness values as measured from a single data acquisition of an isolated point scatterer provide the input to the algorithm and the output is a depth position estimate, corresponding to the PDF maximum. The method does not result in a separate PSF and the PDF can be used to assess its performance. First, the accuracy of the normalized sharpness method is indicated by the depth deviation of the method's z-estimate to the actual scatterer position, d_{dev}. The true scatterer position is known for all simulations and is established from a high precision translation stage during the experimental measurements. Depth estimates for all acquired datasets are calculated and compared with the actual positions. For v repetitive measurements, d_{dev} results from the Root Mean Square Error (RMSE) from all v cases. The average d_{dev} is calculated for the total scatterer displacement and several smaller depth ranges, as in the optics equivalent [44]. Second, the Full-Width-at-Half-Maximum (FWHM) of the PDF is calculated in each depth position and similar to the d_{dev} analysis, average PDF FWHM values are also extracted. They are compared with the corresponding axial FWHM measured by the PSFs of the DAS beamformed responses [see Fig. 1(b)], providing a comparable metric with the conventional localization limits. Third, the standard deviation d_{SD}, of the average d_{dev}, and the standard deviation (FWHM$_{SD}$), of the average PDF FWHM are calculated as extra indicators of the measurements' uncertainty. Fig. 2 shows an example of how a single PDF leads to individual d_{dev} and FWHM estimations, for a scatterer located at a depth of 40 mm. The DAS axial FWHM assessment by the signal envelope is also included in the top right part of the figure.

E. Simulation of Point Scatter

The ultrasound field simulation package Field II [47], [48] was used to model the multiple focusing requirement. A phantom consisting of a single point scatterer at a depth of 40 mm, was created and used as a target to replicate the optical setup. The phantom was scanned by single Plane Wave (PW) emissions, made by a 7 MHz, 192 element, linear array simulated transducer with λ spacing. The central transducer element was located above the point target. The speed of sound, c was set to 1540 m/s and all the parameters, for both simulation and experimental data discussed below, are given in Table I.

Raw data from a single unfocused emission were acquired from all 192 channels individually in receive. The data were stored, and the process was then repeated for 151 axial displacement steps of 100 μm from position 32.5 mm to 47.5 mm. For the initial investigation, noise-free sharpness data were used. To introduce the uncertainty necessary for the PDF calculation, white Gaussian noise was later added to the raw simulated signals. Ten sharpness datasets were created with a Signal-to-Noise Ratio (SNR) equal to 10 dB. For each acquisition the data were beamformed with three different foci in receive. The central receive focus was selected at a depth of 40 mm, the target's initial position, and then the two other values were at −2 mm and +2 mm of the starting depth. The sharpness values were calculated from an area with dimensions 1.3 mm × 1.3 mm
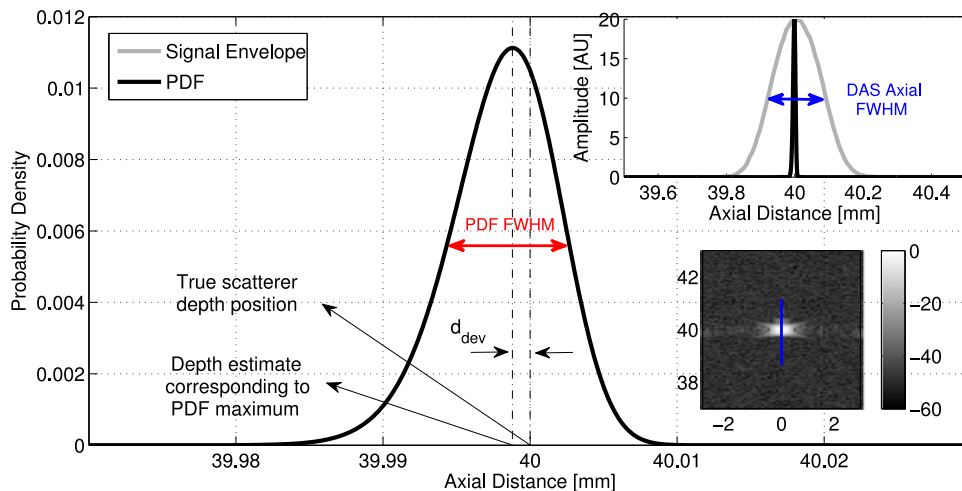
Fig. 2. An exemplary PDF of the normalized sharpness method plotted over depth for a simulated scatterer located at 40 mm depth. The d_{dev} and PDF FWHM measures used for the performance evaluation are shown. The PSF of the scatterer is displayed in the 6 mm × 6 mm image on the right, and a 60 dB dynamic range display was used. On top right the signal envelope from the PSF centre is plotted over depth and the DAS axial FWHM is indicated. The PDF was scaled to the maximum envelope amplitude and was also included for comparison.

TABLE I
SIMULATION AND EXPERIMENTAL SCAN PARAMETERS

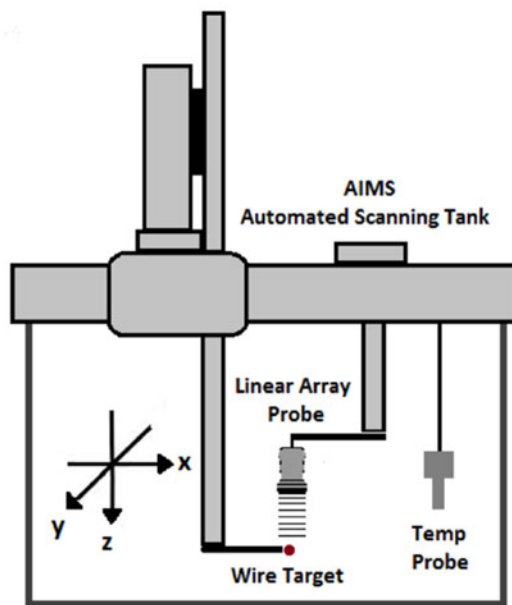| Parameter name	Simulation	Experiment
Transducer type	Linear array	
Transducer element pitch	208 μm	
Transducer element kerf	35 μm	
Transducer element height	4.5 mm	
Centre frequency, f_0	7 MHz	
Sampling frequency, f_s	100 MHz	70 MHz
Bandwidth	60% fractional	
Speed of sound, c	1540 m/s	1484 m/s
Wavelength, $\lambda = c/f_0$	220 μm	212 μm
Excitation pulse	Two-cycle sinusoid at f_0	
Transmit apodization	Hanning	
Receive apodization	Hanning	
Receive focal depths	38 mm/40 mm/42 mm	
Number of transmitting elements	192	
Number of receiving elements, M	192	
Number of emissions	1	
Highest scatterer position	$(x, z) = (0, 32.5)$ mm	
Lowest scatterer position	$(x, z) = (0, 47.5)$ mm	
Total distance covered	15 mm (axially only)	
z-step between 2 emissions	100 μm	108.7 μm
Region of interest (ROI)	1.3 mm × 1.3 mm	2.3 mm × 2.3 mm

Fig. 3. Illustration of the measurement setup: A wire target was inserted into a water tank, which had the Onda AIMS III positioning system attached. The wire was moved from an initial position across the z-dimension and was imaged for every displacement. The SARUS scanner was used for all acquisitions.

around the scatterer centre to fully enclose the defocused PSF main-lobe, but minimize unnecessary background signal.

F. Wire-Target Experiment

For the experimental verification the setup depicted in Fig. 3 was used. A wire with 0.07 mm diameter was attached to a holder rod and was initially positioned at $(x, z) = (0, 40)$ mm, inside a water tank. The custom phantom position was kept fixed in the two dimensions ($x-$ and $y-$axis). After each emission the wire was moved to the next z position in the axial direction using the AIMS III positioning setup (Onda Corporation, Sunnyvale, CA), which was controlled using a Matlab interface.

The accuracy of the setup is at worst equal to the minimum movement step, which is $1/92$ mm $= 10.87$ μm as stated in the equipment manual. The ratio $1/92$ is attributed to the stepper motor system. To avoid potential mechanical inaccuracies with the minimal stepper mode increment, z-steps of 108.7 μm were used. Consequently the total distance of 15 mm was covered in 139 steps. The speed of sound was calculated to $c = 1484$ m/s based on the water temperature [49]. The measurements were performed by the 1024 channel experimental ultrasound scanner SARUS (Synthetic Aperture Real-time Ultrasound System)

(a) 36 mm   (b) 37 mm   (c) 38 mm   (d) 39 mm   (e) 40 mm   (f) 41 mm   (g) 42 mm   (h) 43 mm   (i) 44 mm
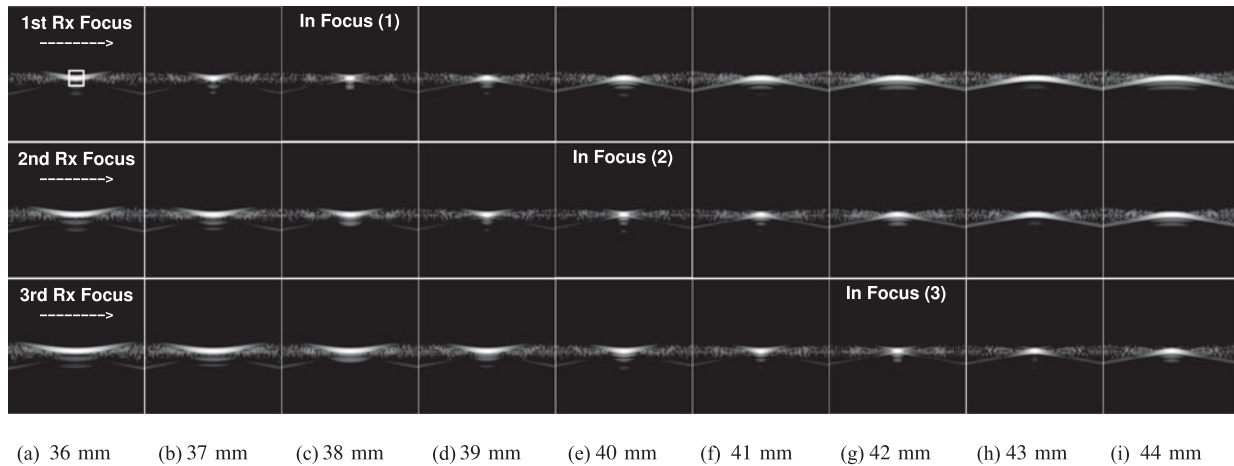
Fig. 4. Point target images at different axial displacement generated by using different receive foci. Columns (a) to (i) represent different depth locations from 36 mm to 44 mm respectively with 1 mm gap between them. Each image covers a 10 mm × 10 mm area. The noise-free simulated dataset was beamformed with three different receive (Rx) foci positioned at 38 mm, 40 mm and 42 mm, shown in the 1st, 2nd and 3rd row respectively. A 60 dB dynamic range display was used. The normalized sharpness was calculated by the envelope detected data samples or the image pixels that are included in the white box with dimensions 1.3 mm × 1.3 mm shown in (a), first row.
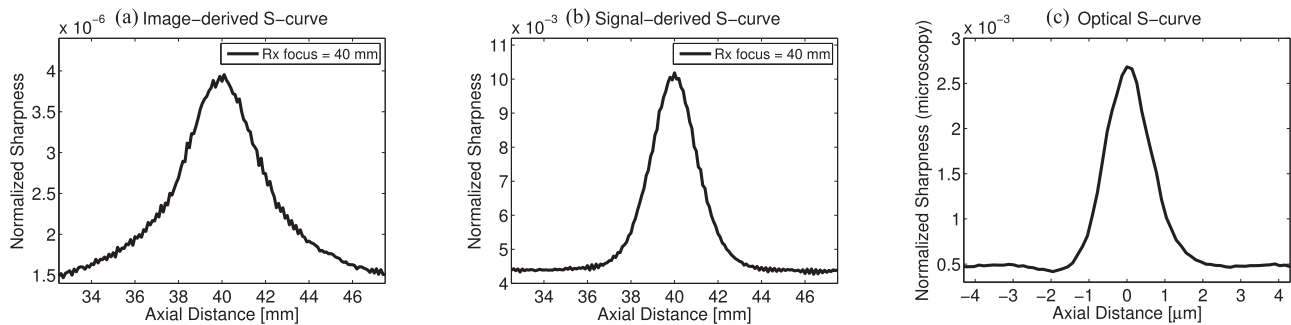
Fig. 5. Normalized sharpness as a function of axial displacement. Image derived sharpness is displayed in (a) for the middle row of the noise-free Field II images shown in Fig. 4 using pixel values for the sharpness calculation. The corresponding signal-derived sharpness is displayed in (b) by using the envelope detected data and (2). In (c) an equivalent result from optical microscopy is shown for comparison.

[50] and a BK Ultrasound (Herlev, Denmark) linear array was used to scan the custom single-wire phantom. Data were initially sampled at 70 MHz as the SARUS scanner requires, and then the sampling frequency, f_s was decimated by a factor of 2 to 35 MHz. All the scan parameters can be found in Table I.

Both simulation and measurement were conducted in a similar manner using similar parameters as indicated in Table I. Transmission of ultrasound was again performed through single plane waves, using all the transducer elements as the transmitting aperture. RF data from one unfocused emission were acquired from all 192 channels individually in receive. Ten frames were acquired per axial position. For each acquisition the data were beamformed in three different foci in receive with the use of an in-house programmed beamformation toolbox BFT III [51]. The receive foci were selected to be at 38 mm, 40 mm, and 42 mm. Data were produced across 15 mm, between 32.5 mm and 47.5 mm from the transducer face. After each set of 10 emissions the data were stored and the wire target was moved to the next location in the axial direction. The ROI was defined, as in the previous subsection, as the smallest area enclosing the PSF main-lobe. This was 2.3 mm × 2.3 mm around the wire centre during the measurement.

III. RESULTS

A. Simulation

From the first, noise-free simulation, the resulting PSFs of a single point scatterer moving in the axial direction are shown in Fig. 4 as a function of point displacement. Similar to [43], Fig. 4 demonstrates the effect of different receive focusing on the PSF appearance. Exemplary S-curves were formed for the ultrasound data corresponding to the central receive focus (40 mm). Sharpness was calculated at each displacement, using (1) without the bias term $-n_k$ in Fig. 5(a), and using (2) in Fig. 5(b). For interest, the curves in Fig. 5 are displayed alongside an S-curve derived from optical confocal microscopy data in Fig. 5(c). This was generated by a setup that included a spatial pinhole with a diameter of 1 Airy unit [52] that was positioned at the confocal plane of the lens used to image a red fluorosphere with a diameter of 100 nm moved through an axial defocus range by equivalent z-stage scanning. The optical wavelength was equal to 650 nm and the total displacement 8 μm for the fluorescent particle. The pinhole addition results into the elimination of out-of-focus light and provides a close approximation to the focused ultrasound upon receive which is used here as shown in Fig. 1(b).
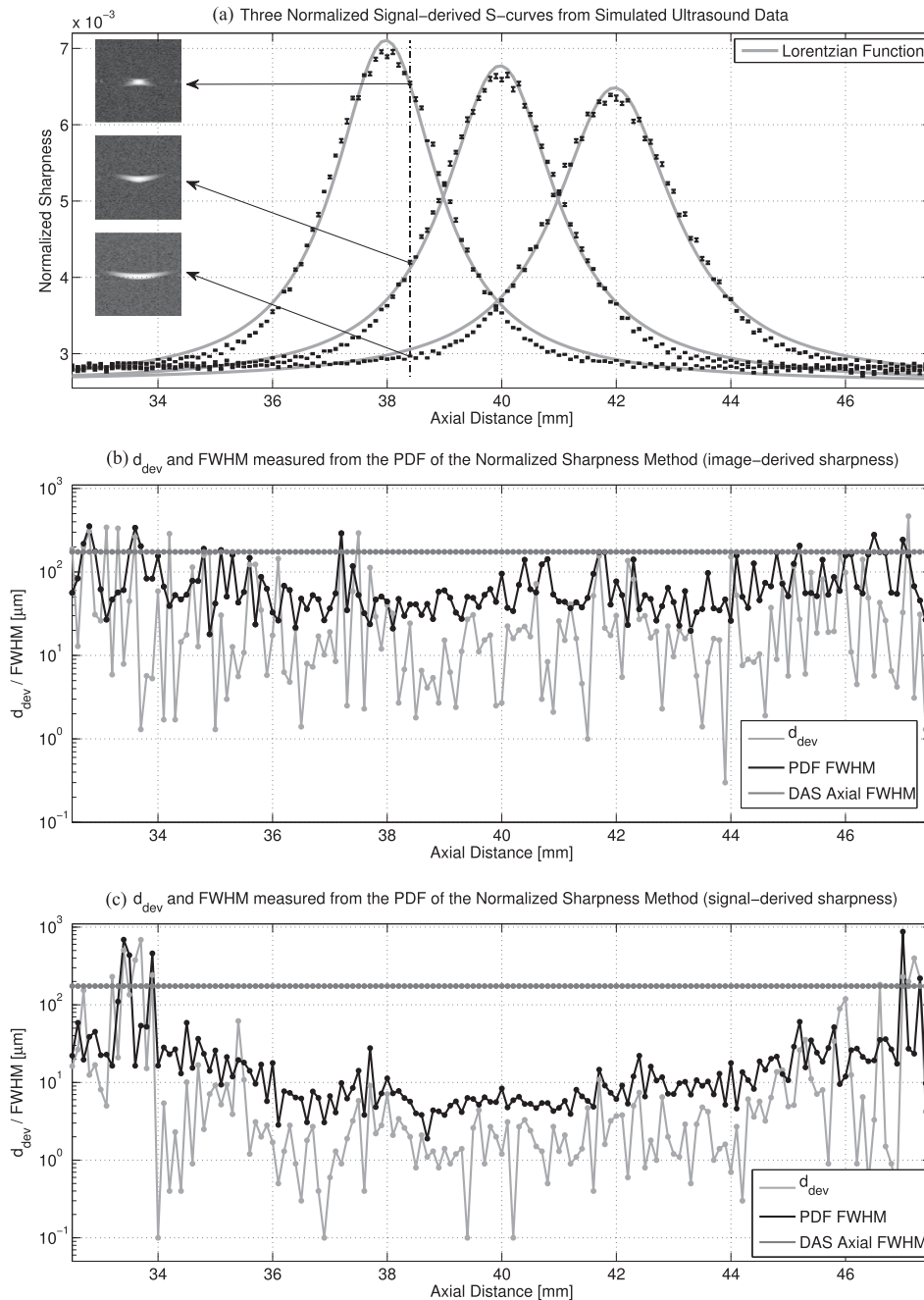
Fig. 6. (a) A set of three normalized S-curves and their Lorentzian fits are displayed. These were generated using a simulated ultrasound point target that is moving in the depth direction, and an unfocused PW ultrasound transmission that was beamformed using three different foci in receive (at 38 mm, 40 mm and 42 mm respectively). The mean sharpness values for a single axial position at 38.4 mm were measured from the 3 PSFs shown on the left, as an example (see text for sharpness values). Each beamformed response corresponds to each receive focus and to that specific depth position. The d_{dev} and the PDF FWHM achieved by the normalized sharpness method are shown in (b) for image-derived sharpness and in (c) for signal-derived sharpness, for each depth position. The dark gray lines in (b) and (c) indicate the DAS axial FWHM.

The general shape of all S-curves shown in Fig. 5 is similar, maximizing at a single peak around the focus, and falling rapidly, and roughly symmetrically with defocus. This provides confidence that the established multi-focal sharpness method is translatable from optical to ultrasound imaging. The signal-derived S-curve [see Fig. 5(b)] is falling more rapidly than the image-derived S-curve [see Fig. 5(a)], and the higher rate of change noticed in Fig. 5(b) increases the sensitivity when using

the MLE. For the calculation of each of the ultrasound signal-derived sharpness values, 12×169 envelope detected data samples were processed corresponding to the $1.3 \, \text{mm} \times 1.3 \, \text{mm}$ ROI. The same region was represented by 45×45 square pixels of image data.

The introduction of noise to the RF signals allowed the generation of a calibration standard based on the calculation of mean sharpness values and their standard deviation, for use with the

MLE analysis. In Fig. 6(a) the mean sharpness was plotted over axial displacement for the three receive foci (38 mm, 40 mm, 42 mm). The best Lorentzian fits of the 3 sharpness datasets were also included in Fig. 6(a). The fits are not meant as accurate representations of the sharpness function, however, they return correlation coefficient, r values, higher than 0.97 for all 3 cases between fitted and S-curves, allowing, in this example, for a good approximation. The error bar represents the sharpness standard deviation in each depth. The displayed data resulted from ten Field II simulations in each z-position as explained in Section II-E. Each curve's peak was located around the position of each receive focus. As an example, a set of 3 PSFs from each focal plane for a single axial position at 38.4 mm, were also shown. Each image was 6 mm × 6 mm and a 60 dB dynamic range display was used. Mean sharpness values were calculated from the displayed PSFs, to 6.548×10^{-3} ($\pm 6 \times 10^{-6}$), 4.197×10^{-3} ($\pm 6 \times 10^{-6}$) and 2.972×10^{-3} ($\pm 2 \times 10^{-6}$) for the 1st, 2nd and 3rd receive focus respectively.

Fig. 6(b) and (c) show the theoretical accuracy in the scatterer axial localization based on the image- and signal-derived sharpness values respectively, the MLE method and the metrics described in Section II-D. The image-derived sharpness processing resulted in an average depth deviation to actual scatterer position (d_{dev}) equal to 47.43 μm ($\approx \lambda/5$) for the whole depth range between 32.5 mm and 47.5 mm. The standard deviation of the d_{dev} (d_{SD}) was equal to 79.66 μm ($\approx \lambda/3$). This is because several low-precision depth estimates ($d_{dev} \cong \lambda$) were included in the calculation. The calculated PDF FWHM was on average equal to 78.67 μm ($\approx \lambda/3$) which is 2.2 times lower than the DAS axial FWHM (170.35 μm) that is always constant regardless of scatterer or receive focus position. The corresponding standard deviation of the PDF FWHM (FWHM$_{SD}$) was 63.37 μm ($\approx \lambda/3.5$). These metrics improve significantly for the signal-derived sharpness processing [see Fig. 6(c)]. For the same range the average d_{dev} was calculated to 29.4 μm ($\approx \lambda/7.5$), and the d_{SD} to 91.47 μm ($\approx \lambda/2.5$). In a similar manner, the average PDF FWHM was calculated to 32.56 μm ($\approx \lambda/7$) which is 6.8 times lower than the DAS axial FWHM, and the FWHM$_{SD}$ to 103.42 μm ($\approx \lambda/2$). In general, the high standard deviation values are due to the increased d_{dev} and PDF FWHM values at regions of reduced rate of sharpness change such as the displacement edges or the S-curve peaks [see Fig. 6(a)]. This is a feature in common with the optical equivalent and it is worth comparing two smaller ranges in the ultrasound analogue. For instance, the 1 mm range between 37.5 mm and 38.5 mm is far from both displacement ends and includes the peak of the first S-curve around the 38 mm receive focus and the lower parts of the other two S-curves' slopes. For this range the average d_{dev} was equal to 3.48 μm, the d_{SD} was 2.72 μm, the average PDF FWHM was 9.1 μm and the FWHM$_{SD}$ was 6.91 μm. The 1 mm range between 38.5 mm and 39.5 mm includes the maximum rate of sharpness change for the S-curves corresponding to the first two receive foci (38 mm and 40 mm) and the lower part of the S-curve slope corresponding to the longest receive focus (42 mm). For the second small range, the average d_{dev} was as low as 1.25 μm, the d_{SD} was 0.67 μm, the average PDF FWHM was 4.5 μm and the FWHM$_{SD}$ was 1.26 μm. These

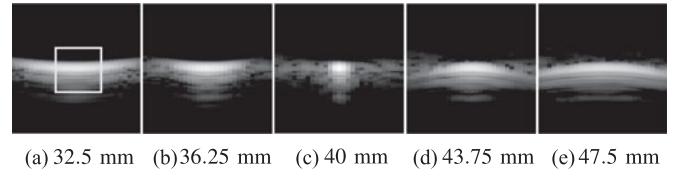(a) 32.5 mm (b) 36.25 mm (c) 40 mm (d) 43.75 mm (e) 47.5 mm

Fig. 7. Five PSFs corresponding to maximum, middle and zero displacements for both ends, during the wire-target experiment. The receive focus was set to 40 mm. Each image includes an area of 6 mm × 6 mm and a 60 dB dynamic range display was used. The normalized sharpness was calculated by the RF samples included in the white box with dimensions 2.3 mm × 2.3 mm shown in (a).

results show that by avoiding the S-curve edges and focusing on the slopes the performance of the method improves greatly, while the inclusion of a peak slightly compromises the accuracy of the localization, and this is consistent with other such sub-ranges across the entire displacement investigated here.

B. Wire-Target Experiment

Five experimentally acquired PSFs of a wire-target moving in the axial direction from a single plane (receive focus = 40 mm) are shown in Fig. 7 in different axial displacements. The figure is equivalent to Fig. 4 (2nd row) and the receive beamforming was expanded to two further receive foci (38 mm and 42 mm), as in the simulation. In Fig. 8(a), the measured mean sharpness was plotted over axial displacement and the best Lorentzian S-curve fits ($r > 0.98$) were also added. The error bar represents the sharpness standard deviation for each depth. The displayed sharpness data resulted from 10 experimentally acquired frames in each z-position. Each curve's peak was located around the position of each receive focus. The set of 3 PSFs from $z = 38.37$ mm are also shown as an example. Each image is 6 mm × 6 mm and a 60 dB dynamic range display was used. The mean sharpness values were calculated to 8.491×10^{-3} ($\pm 1.4 \times 10^{-5}$), 5.938×10^{-3} ($\pm 9 \times 10^{-6}$) and 4.053×10^{-3} ($\pm 6 \times 10^{-6}$) for the 1st, 2nd and 3rd receive focus respectively.

Fig. 8(b) and (c) show the accuracy in the wire axial localization based on the sharpness processing for image- and signal-derived sharpness respectively. As in the simulation study, the use of the envelope detected data for the sharpness calculation outperformed the image sharpness processing. The latter resulted in an average d_{dev} equal to 63.67 μm (or $\approx \lambda/3$). The d_{SD} was equal to 102.35 (or $\approx \lambda/2$) due to several d_{dev} values higher than the wavelength (212 μm), located at the displacement edges. The calculated PDF FWHM was on average equal to 83.91 μm ($\approx \lambda/2.5$) which is 3.4 times lower than the DAS axial FWHM, which was measured to 287.31 μm from the signal envelope that passes through the centre of the PSF as shown in Fig. 2. The corresponding FWHM$_{SD}$ was 83.86 μm ($\approx \lambda/2.5$). For the signal-derived sharpness the average d_{dev} was calculated to 10.21 μm (or $\approx \lambda/21$). The d_{SD} for the entire depth range was calculated to 16.11 μm (or $\approx \lambda/13$), indicating smaller variations between the d_{dev} values compared to the simulation study. The average PDF FWHM was calculated to
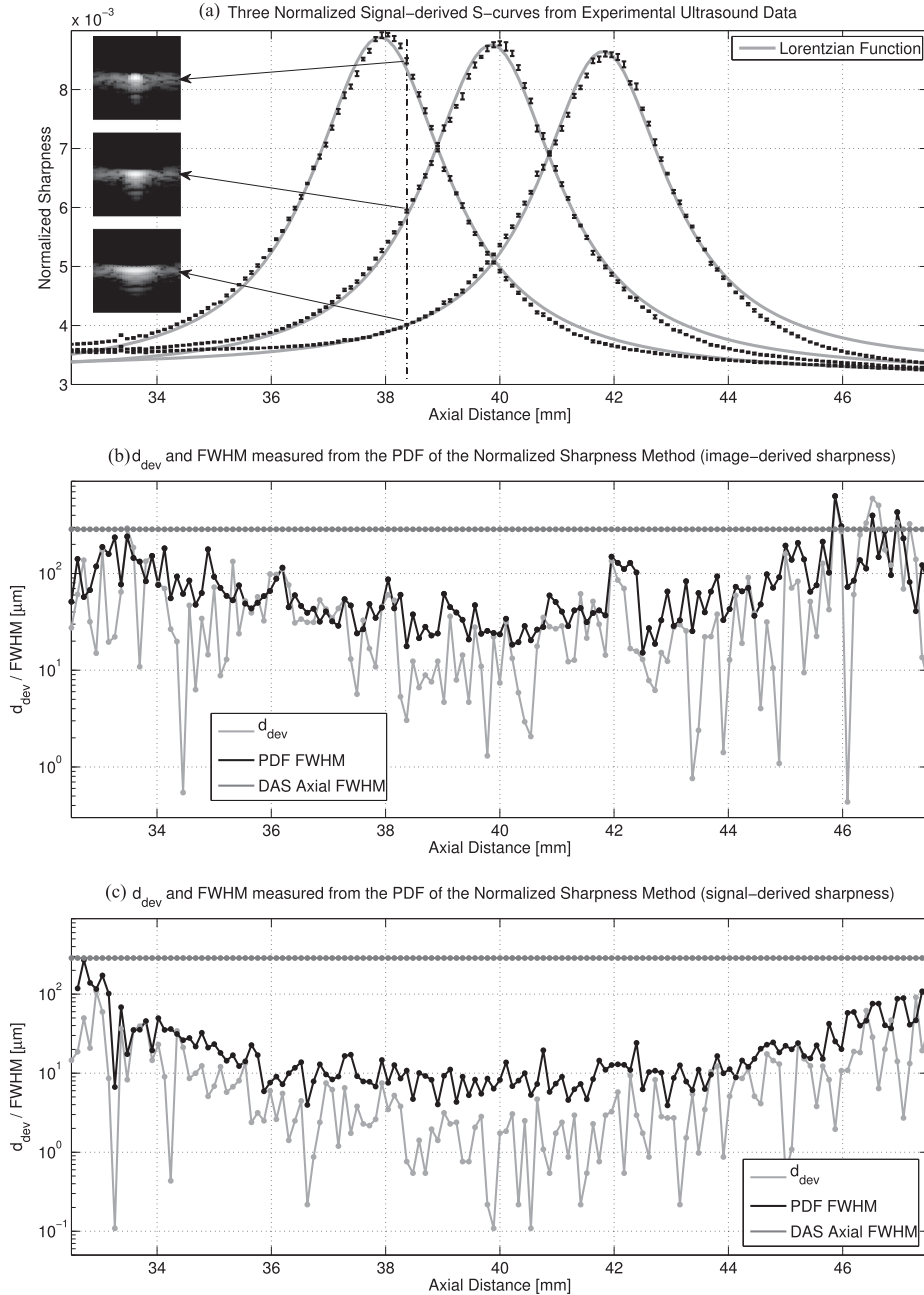
Fig. 8. (a) A set of three normalized S-curves and their Lorentzian fits are displayed. These were generated using a wire-target that is moving in the depth direction, and an unfocused PW ultrasound transmission that was beamformed using three different foci in receive (at 38 mm, 40 mm and 42 mm respectively). The mean sharpness values for a single axial position at 38.37 mm were measured from the 3 PSFs shown on the left, as an example (see text for sharpness values). Each beamformed response corresponds to each receive focus and to that specific depth position. The d_{dev} and the PDF FWHM achieved by the normalized sharpness method are shown in (b) for image-derived sharpness and in (c) for signal-derived sharpness, for each depth position. The dark gray lines in (b) and (c) indicate the DAS axial FWHM.

$25.15\,\mu$m ($\approx \lambda/8.5$) which is 11.4 times lower than the DAS axial FWHM, and the FWHM$_{SD}$ was $35.09\,\mu$m ($\approx \lambda/6$).

The two 1 mm ranges were also investigated as in the simulation study. For the 1 mm depth range between 37.5 mm and 38.5 mm, the average d_{dev} was equal to $3.22\,\mu$m, the d_{SD} was $2.07\,\mu$m, the average PDF FWHM was $9.06\,\mu$m and the FWHM$_{SD}$ was $2.93\,\mu$m. The 1 mm range between 38.5 mm and 39.5 mm resulted in slightly lower values for the same metrics, confirming the benefits of examining areas where the sharpness changes rapidly. An average d_{dev} equal to $1.52\,\mu$m was cal-

culated, the d_{SD} was $0.90\,\mu$m, the average PDF FWHM was $7.53\,\mu$m and the FWHM$_{SD}$ was $2.66\,\mu$m.

IV. DISCUSSION

The principle of multi-focal axial ultrasound localization has been demonstrated through the use of the sharpness metric applied to simulated and experimental point scatter data. While a large number of beamforming methods [30], [53], [54] have shown significant localization gains in the lateral ultrasound ar-

ray dimension, this is the first beamforming technique to show significant gain in the axial direction. The proposed method exploits the effect of defocus on the diffraction-limited lateral resolution to achieve high precision localization in the axial dimension, and is based on a previously presented method for super-resolution optical microscopy [43], [44]. In optics, in the absence of other aberrations, sharpness is purely dependent on defocus. The influence of defocus aberration on the PSF shape is similar for optics and ultrasonics, which enabled the translation of the technique. The only difference is in the wavelengths ($\sim$500 nm for optics compared to $\sim$200 μm for ultrasonics), which resulted in nanometre ($\approx$10 nm) and micrometre ($\approx$10 μm) depth localization precision, respectively.

A 25% lower depth deviation (d_{dev}) to actual scatterer position was acquired in simulation (47.43 μm) compared to experiment (63.67 μm) for the image-derived sharpness analysis. However, the processing that utilizes image data is less reliable as described in Section III-A, and overall resulted in limited localization improvements for both simulation and experiment. The signal-derived sharpness analysis showed improved performance by a factor of $\approx$3 for the wire-target measurements (10.21 μm) compared to the simulated scatterer (29.4 μm), with both d_{dev} values significantly lower than those obtained from image data. The difference between simulation and experimental studies is attributed to the nature and amplitude of the noise added to the simulated data. The noise was assumed Gaussian as common practice for most noise processes and higher than in the experimental case, providing increased d_{dev} near to the displacement edges, and subsequently a higher d_{SD}.

Similar conclusions were drawn from the introduction of the average PDF FWHM and its standard deviation as performance metrics, which also enabled a comparison with the DAS-derived axial localization (DAS axial FWHM). This is an indirect comparison since the proposed method does not result in a PSF. However it was shown in Fig. 2 that the PDF generated by the sharpness processing can be used to limit the depth position range as this is calculated by the axial PSF size. In simulation the image-derived sharpness analysis provided 7% lower average PDF FWHM (78.67 μm), compared to the experiment (81.93 μm). However this was translated in 2.2- and 3.4-fold improvements compared to the DAS localization, since the DAS axial FWHM was 287.31 μm for the wire-target and 170.35 μm for the simulated point scatterer. The signal-derived sharpness analysis resulted in similar average PDF FWHM values for the simulated scatterer (32.56 μm) and the wire-target measurements (25.15 μm) further increasing the axial localization gains to 6.8- and 11.4-fold respectively. In the experimental case, the FWHM$_{SD}$ was also calculated lower by a factor of $\approx$3 than the one obtained from the simulated data. In addition, the method does not perform uniformly for the whole displacement range. The data analysis of small sub-regions showed that away from the displacement edges and in areas dominated by at least two of the S-curve slopes the technique performs best, achieving axial localization with lower than 3.5 μm precision and an average PDF FWHM up to 38 times lower than the DAS axial FWHM for both simulation and measurement. However, this result is not conclusive and the method needs to develop further in or-

der to identify whether such axial localization accuracy can be achieved consistently for a large range of depths.

In general, the ability of the proposed method to control the sharpness value by altering the time delays could potentially allow its usage for optimum focusing definition or aberration correction applications in ultrasound imaging [45]. However, the obvious application in ultrasound is the depth detection of contrast microbubbles. Current microbubble visualization has enabled the use of localization algorithms on image data. This has typically been accomplished by identifying the PSF centre of mass of spatially isolated bubbles [20], [55] or by fitting three dimensional Gaussians to approximate the PSF and thus estimate the position of the bubble [18], [19], [56], approaches which are inaccurate for axial determination. The method proposed here can be developed to be applied as an adjunct to these techniques. The use of contrast microbubbles will allow translation to real imaging applications where the limiting factor will be SNR and image quality. New image post-processing may stem from combining the conventional lateral appearance of a point target and the sharpness derived axial one. This will have the advantage of improved PSF shape definition in a noiseless meta-image, thus contributing to the optimization of current image based PSF localization. Furthermore, the sharpness method can be considered as an adjunct to other signal-based methods for lateral resolution such as the Minimum Variance beamformer [30], [53], [54]. This may improve localization by providing a much smaller PSF for further analysis by the same image based techniques.

The overall accuracy of the technique and its application to real-time MB imaging depends on a number of factors. First, the MBs are known for their poly-dispersed nature and their signal variation, and the normalization factor from (2) compensates for different MB echo signals. Second, the SNR in MB imaging is not the typical SNR from ultrasound images, but rather the demodulated signal to clutter ratio, after the linear tissue signals have been rejected, using pulse modulation (such as phase or amplitude), to create the MB only image. In these images, MBs tend to be clearly identifiable compared to the dark background and the scatter can be identified in order to implement the sharpness method. The SNR in the current study is better than that available in *in-vivo* imaging, but not significantly. In any case, the impact of SNR on localization accuracy needs to be investigated further in order to explore the potential of the technique for real imaging. Another important aspect of ultrasound imaging is the PSF, and thus SNR variability, across the image. This is due to the signal processing as well as the beam changes that occur due to attenuation and speed of sound variations imposed by real tissues in the near field for the transducer array. This may translate in varying localization accuracy across the image. Further complexity is introduced by the sharpness relation to focus. It is the defocus that minimizes localization error, which appears to counter balance the decrease in the ultrasound image SNR in that range. Third, the MB detection sensitivity may vary as, in addition to SNR, the variable beam pressure across the image provides a variable number of MBs that scatter above noise [16]. Note, that *in-vivo* there is a correlation between MB density with blood volume, and as a result super-resolution contrast

ultrasound imaging aims to generate quantitative blood volume maps. The variation of the ultrasound beam pressure impacts on the relationship between MB number and blood volume and the PSF variation across the image. The PSF may therefore be used as a marker of MB density variation.

Fourth, a single scatterer must be included in the selected ROI for each sharpness calculation as outlined in Section II-A. In a real-time imaging environment an initial rough estimation of scatterers position based on standard DAS beamforming will be followed by the ROI selection. The application of thresholding criteria such as intensity, shape or morphology will need to be implemented to discard echoes that violate the single scatterer requirement. This may be due to the overlapping PSFs or side-lobe contributions from neighboring scatterers. The localization technique will be applied to a single frame and then the whole processing will be repeated for the next frame. The concept is similar to optical microscopy [57]. In case of high MB density, the ROI rejection rate will be high, increasing the number of frames that need to be processed until an adequate number of isolated targets is reached and localized throughout the entire image. As a consequence an efficient ROI size selection is closely related to the single scatterer assumption and the acquisition time. In this work the ROI selection is not significant since there is only a single scatterer in all images. However, it was shown that using the size of the PSF main lobe as reference, is a valid approach in order to achieve a robust ROI selection and potentially maximize the useful ROIs number in a frame. Using the figures presented during the wire-target measurements, a 15 mm $\times$ 15 mm area divided into 2.3 mm $\times$ 2.3 mm boxes could include at most 42 ROIs including an isolated scatterer per frame. The localization of several thousands of MBs would be required for a density map generation. The number of frames will therefore depend on the number of MBs that can practically be detected per frame given a low infusion concentration to achieve isolated MB scatter in the image, and the tissue vascular structure that imposes a varying MB density across the image.

Moreover, the type of ultrasound transmission may have an impact on the method's performance. The plane wave transmission was chosen in this paper, because it is the best approximation to the unfocused light transmission as in the optical measurements. In addition, it facilitates fast acquisitions as only one emission is able to provide all the necessary data for the method and thus is not subject to artefacts due to the particle movement between several emissions that are all used to form one image. However Synthetic Aperture (SA) ultrasound can offer similar benefits. The images acquired from single SA emissions will maintain the same high frame rate, without reducing image quality. The dependence of the sharpness-based localization method on the transmit focus needs to be explored. Focused ultrasound requires a higher number of emissions to produce a single image, but the image quality around the focus area is significantly improved. Considering that apodization also plays an important role in the ultrasound beam shaping, this is another parameter that needs to be explored. However, all the above remain to be investigated. In addition, further research is required for targets that are located at greater depths, or provide lower SNR. Finally, in this paper it was demonstrated how 3

receive foci at 2 mm separation were adequate for a localization precision of 10.21 μm over a displacement range of 15 mm. It is clear that by extending the number of receive foci this range can be increased, and that by optimizing the foci spacing further localization accuracy can be tuned. Ultimately there will be trade-off between depth range, number of foci and foci spacing, which need to be balanced in response to specific imaging problems and systems. In theory an unlimited number of S-curves can be formed, as the receive focus locations can be unlimited. This is a major advantage of the ultrasound implementation of the method compared to the optical equivalent, where hardware challenges limit the number of planes to typically less than 10.

In the end, the method needs to be developed in tissue-like media that provide complex aberrations. Indeed, the PSF of ultrasound is known to be very variable across the image due to varying attenuation and reflections inside the human body. This is not unique to ultrasound. The flickering of the stars is caused by the change of refraction in the atmosphere due to its movement. While this problem is resolved systematically for astronomy using adaptive optics methods [58], it remains for ultrasound imaging, which is a highly operator dependent technique and the image is qualitatively compensated for the variation in the ultrasound field. This may well prove a key advantage of the normalized sharpness method, which does not require an understanding of the exact aberrations or any pre-defined PSF model.

V. CONCLUSION

The defocusing errors of a point scatterer at different axial positions were examined for ultrasound imaging. They were quantified by the metric of normalized sharpness, which becomes maximum for in-focused images and falls spatially roughly symmetrically away from focus. This depth dependence of the sharpness values when plotted together, and the ability in ultrasound imaging to obtain multi-focal images of the same object offer a simple method that provides high-precision axial localization. Experimental results showed that a set of 3 sharpness values was adequate to localize the axial position of a point target with $\approx$10 micrometre accuracy, also reducing the conventional axial Full-Width-at-Half-Maximum (FWHM) by a factor of $\approx$11. This initial investigation showed that the technique is well-suited for ultrasound point scatterers. The technique may complement image-based methods currently used for microbubble detection, or other beamforming techniques focusing in the lateral resolution to fully describe point scatter position based exclusively on signal processing.

REFERENCES

[1] P. Hoskins *et al.*, *Diagnostic Ultrasound: Physics and Equipment*, 2nd ed. Cambridge, U.K.: Cambridge Univ. Press, 2010.

[2] M. L. Oelze and W. D. O. Jr, "Defining optimal axial and lateral resolution for estimating scatterer properties from volumes using ultrasound backscatter," *J. Acoust. Soc. Amer.*, vol. 115, no. 6, pp. 3226–3234, 2004.

[3] J. A. Jensen, "Deconvolution of ultrasound images," *Ultrason. Imag.*, vol. 14, no. 1, pp. 1–15, 1992.

[4] T. Szabo, *Diagnostic Ultrasound Imaging: Inside Out*, 2nd ed. New York, NY, USA: Elsevier, 2013.

[5] D. A. Knapik *et al.*, "A 100–200 MHz ultrasound biomicroscope," *IEEE Trans. Ultrason., Ferroelect., Freq. Control*, vol. 47, no. 6, pp. 1540–1549, Nov. 2000.

[6] F. S. Foster *et al.*, "Advances in ultrasound biomicroscopy," *Ultrasound Med. Biol.*, vol. 26, no. 1, pp. 1–27, Jan. 2000.

[7] C. Errico *et al.*, "Ultrafast ultrasound localization microscopy for deep super-resolution vascular imaging," *Nature Lett.*, vol. 527, no. 7579, pp. 499–502, 2015.

[8] S. Haykin *et al.*, *Array Signal Processing*. Englewood Cliffs, NJ, USA: Prentice-Hall, 1985.

[9] A. Quinquis *et al.*, "Some radar imagery results using superresolution techniques," *IEEE Trans. Antennas Propag.*, vol. 52, no. 5, pp. 1–15, May 2004.

[10] I. J. Clarke *et al.*, "Resolution limits of a two dimensional antenna array," *Proc. SPIE Real-Time Signal Process. VIII*, vol. 0564, pp. 0564-0564-8, Jan. 1986, doi: 10.1117/12.949698.

[11] I. J. Clarke and G. Spence, "A space-time estimator for the detection and estimation of multiple sinusoidal signals," in *Proc. IEE Colloq. High Resolution Radar Sonar*, 1999, pp. 9/1–9/6.

[12] K. G. Puschmann and F. Kneer, "On super-resolution in astronomical imaging," *Astron. Astrophys.*, vol. 436, no. 1, pp. 373–378, 2005.

[13] S. T. Hess *et al.*, "Ultra-high resolution imaging by fluorescence photoactivation localization microscopy," *Biophys. J.*, vol. 91, no. 11, pp. 4258–4272, 2006.

[14] S. Djidel *et al.*, "High-speed, 3-dimensional, telecentric imaging," *Opt. Express*, vol. 14, no. 18, pp. 8269–8277, 2006.

[15] M. Bates *et al.*, "Multicolor super-resolution imaging with photoswitchable fluorescent probes," *Science*, vol. 317, no. 5845, pp. 1749–1753, 2007.

[16] V. Sboros *et al.*, "The behaviour of individual contrast agent microbubbles," *Ultrasound Med. Biol.*, vol. 29, no. 5, pp. 687–694, 2003.

[17] R. J. Eckersley *et al.*, "Microbubble contrast agent detection using binary coded pulses," *Ultrasound Med. Biol.*, vol. 33, no. 11, pp. 1787–1795, 2007.

[18] M. A. O'Reilly and K. Hynynen, "A super-resolution ultrasound method for brain vascular mapping," *Med. Phys.*, vol. 40, no. 11, 2013, Art. no. 110701.

[19] M. A. O'Reilly *et al.*, "Three-dimensional transcranial ultrasound imaging of microbubble clouds using a sparse hemispherical array," *IEEE Trans. Biomed. Eng.*, vol. 61, no. 4, pp. 1285–1294, Apr. 2014.

[20] K. Christensen-Jeffries *et al.*, "*In vivo* acoustic super-resolution and super-resolved velocity mapping using microbubbles," *IEEE Trans. Med. Imag.*, vol. 34, no. 2, pp. 433–440, Feb. 2015.

[21] O. Couture *et al.*, "Microbubble ultrasound super-localization imaging (MUSLI)," in *Proc. IEEE Ultrason. Symp.*, 2011, pp. 1285–1287.

[22] M. Tanter and M. Fink, "Ultrafast imaging in biomedical ultrasound," *IEEE Trans. Ultrason., Ferroelect., Freq. Control*, vol. 61, no. 1, pp. 102–119, Jan. 2014.

[23] Y. Desailly *et al.*, "Sono-activated ultrasound localization microscopy," *Appl. Phys. Lett.*, vol. 103, no. 17, 2013, Art. no. 174107.

[24] Y. Desailly *et al.*, "Resolution limits of ultrafast ultrasound localization microscopy," *Phys. Med. Biol.*, vol. 60, no. 22, pp. 8723–8740, 2015.

[25] D. Ackermann and G. Schmitz, "Detection and tracking of multiple microbubbles in ultrasound b-mode images," *IEEE Trans. Ultrason., Ferroelect., Freq. Control*, vol. 63, no. 1, pp. 72–82, Jan. 2016.

[26] M. Fink, "Time reversal of ultrasonic fields-part I: Basic principles," *IEEE Trans. Ultrason., Ferroelect., Freq. Control*, vol. 39, no. 5, pp. 555–566, Sep. 1992.

[27] O. Couture *et al.*, "Time-reversal focusing of therapeutic ultrasound on targeted microbubbles," *Appl. Phys. Lett.*, vol. 94, 2009, Art. no. 173901.

[28] M. Pernot *et al.*, "Ultrasonic stars for time-reversal focusing using induced cavitation bubbles," *Appl. Phys. Lett.*, vol. 88, 2006, Art. no. 034102.

[29] K. Diamantis *et al.*, "A comparison between temporal and subband minimum variance adaptive beamforming," *Proc. SPIE Med. Imag.*, vol. 9040, Mar. 2014, Art. no. 90400L, doi: 10.1117/12.2043602.

[30] K. Diamantis *et al.*, "Experimental performance assessment of the subband minimum variance beamformer for ultrasound imaging," *Ultrasonics*, vol. 79, pp. 87–95, 2017.

[31] S. Cho *et al.*, "Phantom and in vivo evaluation of sound speed estimation methods: Preliminary results," in *Proc. IEEE Ultrason. Symp.*, Sep. 2014, pp. 1678–1681.

[32] H. Taki *et al.*, "High range resolution ultrasonographic vascular imaging using frequency domain interferometry with the Capon method," *IEEE Trans. Med. Imag.*, vol. 31, no. 2, pp. 417–429, Feb. 2012.

[33] J. P. Asen *et al.*, "Implementing Capon beamforming on a GPU for real-time cardiac ultrasound imaging," *IEEE Trans. Ultrason., Ferroelect., Freq. Control*, vol. 61, no. 1, pp. 76–85, Jan. 2014.

[34] X. Qu *et al.*, "Nanometer-localized multiple single-molecule fluorescence microscopy," *Proc. Nat. Acad. Sci. USA*, vol. 101, no. 31, pp. 11298–11303, 2004.

[35] A. L. McEvoy *et al.*, "Q&A: Single-molecule localization microscopy for biological imaging," *BMC Biol.*, vol. 8, no. 106, pp. 1–9, 2010.

[36] Y. Sun *et al.*, "Parallax: High accuracy three-dimensional single molecule tracking using split images," *Nano Lett.*, vol. 9, no. 7, pp. 2676–2682, 2009.

[37] M. Speidel *et al.*, "Three-dimensional tracking of fluorescent nanoparticles with subnanometer precision by use of off-focus imaging," *Opt. Lett.*, vol. 28, no. 2, pp. 69–71, 2003.

[38] G. A. Lessard *et al.*, "Three-dimensional tracking of individual quantum dots," *Appl. Phys. Lett.*, vol. 91, no. 22, 2007, Art. no. 224106.

[39] R. A. Muller and A. Buffington, "Real-time correction of atmospherically degraded telescope images through image sharpnening," *J. Opt. Soc. Amer.*, vol. 64, no. 9, pp. 1200–1210, Sep. 1974.

[40] M. Subbarao and J.-K. Tyan, "Selecting the optimal focus measure for autofocusing and depth-from-focus," *IEEE Trans. Pattern Anal. Mach. Intell.*, vol. 20, no. 8, pp. 864–870, Aug. 1998.

[41] N. K. Chern *et al.*, "Practical issues in pixel-based auto focusing for machine vision," in *Proc. IEEE Robot. Autom.*, May 2001, pp. 2791–2796.

[42] P. M. Blanchard and A. H. Greenaway, "Simultaneous multiplane imaging with a distorted diffraction grating," *Appl. Opt.*, vol. 38, no. 32, pp. 6692–6699, 1999.

[43] P. A. Dalgarno *et al.*, "Multiplane imaging and three dimensional nanoscale particle tracking in biological microscopy," *Opt. Express*, vol. 18, no. 2, pp. 877–884, 2010.

[44] H. I. C. Dalgarno *et al.*, "Nanometric depth resolution from multi-focal images in microscopy," *J. Roy. Soc. Interface*, vol. 8, no. 60, pp. 942–951, Jul. 2011.

[45] L. Nock *et al.*, "Phase aberration correction in medical ultrasound using speckle brightness as a quality factor," *J. Acoust. Soc. Amer.*, vol. 85, no. 5, pp. 1819–1833, 1989.

[46] K. E. Thomenius, "Evolution of ultrasound beamformers," in *Proc. IEEE Ultrason. Symp.*, Nov. 1996, vol. 2, pp. 1615–1622.

[47] J. A. Jensen and N. B. Svendsen, "Calculation of pressure fields from arbitrarily shaped, apodized, and excited ultrasound transducers," *IEEE Trans. Ultrason., Ferroelectr., Freq. Control*, vol. 39, no. 2, pp. 262–267, Mar. 1992.

[48] J. A. Jensen, "Field: A program for simulating ultrasound systems," *Med. Biol. Eng. Comput.*, vol. 34, Suppl. 1, Pt. 1, pp. 351–353, 1996.

[49] W. Marczak, "Water as a standard in the measurements of speed of sound in liquids," *J. Acoust. Soc. Amer.*, vol. 102, no. 5, pp. 2776–2779, 1997.

[50] J. A. Jensen *et al.*, "Sarus: A synthetic aperture real-time ultrasound system," *IEEE Trans. Ultrason., Ferroelect., Freq. Control*, vol. 60, no. 9, pp. 1838–1852, Sep. 2013.

[51] J. M. Hansen *et al.*, "An object-oriented multi-threaded software beam formation toolbox," *Proc. SPIE Med. Imag.*, vol. 7968, Mar. 2011, Art. no. 79680Y, doi: 10.1117/12.878178.

[52] J. B. Pawley, *Handbook of Biological Confocal Microscopy*, 3rd ed. Berlin, Germany: Springer, 2006.

[53] J. F. Synnevåg *et al.*, "Adaptive beamforming applied to medical ultrasound imaging," *IEEE Trans. Ultrason., Ferroelect., Freq. Control*, vol. 54, no. 8, pp. 1606–1613, Aug. 2007.

[54] I. K. Holfort *et al.*, "Broadband minimum variance beamforming for ultrasound imaging," *IEEE Trans. Ultrason., Ferroelect., Freq. Control*, vol. 56, no. 2, pp. 314–325, Feb. 2009.

[55] O. M. Viessmann *et al.*, "Acoustic super-resolution with ultrasound and microbubbles," *Phys. Med. Biol.*, vol. 58, no. 18, pp. 6447–6458, 2013.

[56] M. A. O'Reilly *et al.*, "Investigating a method for non-invasive ultrasound aberration correction through the skull bone," *Proc. SPIE Med. Imag.*, vol. 9040, Mar. 2014, Art. no. 904013, doi: 10.1117/12.2043832.

[57] P. Křížek *et al.*, "Minimizing detection errors in single molecule localization microscopy," *Opt. Express*, vol. 19, no. 4, pp. 3226–3235, 2011.

[58] C. A. Primmerman *et al.*, "Atmospheric-compensation experiments in strong-scintillation conditions," *Appl. Opt.*, vol. 34, no. 12, pp. 2081–2088, 1995.